Hindawi
Shock and Vibration
Volume 2018, Article ID 6142386, 12 pages
https://doi.org/10.1155/2018/6142386

Research Article

Study on Dynamic Characteristics of Aerostatic Bearing with Elastic Equalizing Pressure Groove

Xiao-long Zhao, Hao Dong, Zhou Fang, Deng-di Chen, and Jun-an Zhang

School of Mechatronic Engineering, Xi'an Technological University, Xi'an, Shaanxi 710021, China

Correspondence should be addressed to Jun-an Zhang; zja128@163.com

Received 16 April 2018; Accepted 12 June 2018; Published 26 July 2018

Academic Editor: Luca Landi

Copyright © 2018 Xiao-long Zhao et al. This is an open access article distributed under the Creative Commons Attribution License, which permits unrestricted use, distribution, and reproduction in any medium, provided the original work is properly cited.

Microvibration has an important influence on the dynamic performance of aerostatic bearings. Dynamic stiffness and equivalent damping coefficient are the main indexes to evaluate the dynamic characteristics of the aerostatic bearing. In order to study the dynamic characteristics of a new type of aerostatic bearing with the elastic equalizing pressure groove (EEPG), the dynamic characteristics of the new type of bearing are studied by theoretical calculation and experiment. First, the dynamic gas-solid coupling control equation is established. Then, the steady term and the perturbation term are decomposed by the perturbation method. By solving the coupling model, the dynamic characteristics of the bearing are calculated and analyzed. The calculation results show that the perturbation frequency has a significant effect on the dynamic stiffness and equivalent damping coefficient of the aerostatic bearing with EEPG. The dynamic stiffness increases with the increase of frequency, and the equivalent damping coefficient decreases with the increase of frequency. The experimental results are basically the same with the theoretical results, which effectively verify the correctness of the theoretical analysis.

1. Introduction

Aerostatic bearing is widely used in precision and ultraprecision testing equipment due to its small friction and fast response speed. Because of the compressible nature of air, the aerostatic bearing found it difficult to obtain high bearing capacity and stiffness, which restricts the wide application of aerostatic bearings [1, 2]. Bearing capacity and stiffness belong to the static performance of aerostatic bearings, and the research is relatively sufficient on how to improve the static characteristics of bearings. The study of static characteristics is mainly analyzed by numerical simulation and experimental method, which mainly focuses on the influence of the structure of the throttle, the geometric size optimization, and the flow of gas [3, 4]. During the loading process, the air film of the aerostatic bearing is easily affected by the shock and vibration of the outside, which leads to the obvious weakening of the working stability of the aerostatic bearing [5]. Therefore, the analysis and study of the dynamic characteristics of the bearing are particularly important when it is affected by the external impact.

Some scholars have done some research on the dynamic characteristics of the aerostatic bearing. Nishio et al. [6] have studied the dynamic and static characteristics of the aerostatic bearings with small throttle holes. Through numerical simulation, the flow coefficient of small throttle holes is obtained. Finally, it is pointed out that the stiffness and damping coefficient of the aerostatic bearings with small throttle holes are larger than those of the composite throttling holes. Yadav et al. [7] proposed a new method of calculating the film stiffness and damping coefficient of the aerostatic thrust bearing based on the finite element method

and analyzed the dynamic performance of the static pressure thrust bearing under different concave cavity geometries. Cui et al. [8] analyzed the three-dimensional flow field characteristics of the bearing micro gas film gap and the effect of the gas redundancy on the dynamic stability of the hydrostatic bearing and tested the static and dynamic characteristics of the aerostatic bearing. Guo [9] and others have studied the dynamic performance of the annular throttle aerostatic bearing by numerical calculation. By using the small parameter perturbation and Galerkin finite element method, an approximate solution to the two-dimensional unsteady Reynolds gas lubrication equation in the cylindrical coordinate system is obtained. Chen et al. [10, 11] studied the dynamic stiffness and damping coefficient of the aerostatic bearing and pointed out that the frequency dependence of the dynamic performance of the bearing is more obvious under the micro gas film gap and the high gas supply pressure. Some other scholars have also studied the dynamic characteristics of aerostatic bearings [12–14].

In summary, compared with the static characteristics of the aerostatic bearing, the research on dynamic characteristics is less. The previous research objects are mostly concentrated on the aerostatic bearing with the rigid equalizing pressure groove, and the research on the dynamic characteristics of the new type of aerostatic bearing with EEPG has not been found. Therefore, the dynamic control equation of gas-solid coupling is set up in this paper. A dynamic test bench is also set up. The dynamic characteristics of the new bearing are studied by numerical analysis and experiment. The influence of different perturbation frequencies on the dynamic performance of the bearing is analyzed and summarized, which provides a basis for further research on this bearings.

2. Numerical Calculation Method

2.1. Physical Model. The new aerostatic bearing model with EEPG is shown in Figure 1 [15]. Figure 1(a) shows the physical model of the bearing, Figure 1(b) shows the physical map of the bearing, and Figure 1(c) shows the schematic diagram of the deformation of the EEPG. Among them, the radius of the bearing is R, the ring EEPG is on the bearing surface, and its width is $r2 - r1$. Four throttling holes with a diameter of d are evenly distributed on the EEPG. Figure 1(a) shows the depth value of the initial EEPG. With the increase (or decrease) of the gas film gap h, the difference between the gas supply pressure and the gas film pressure distribution increases (or decreases), forcing the depth of the EEPG to change, which affects the static and dynamic characteristics of the aerostatic bearing. Figures 1(b) and 1(c) show the deformation of EEPG under different gas film gaps.

2.2. Gas-Solid Coupling Control Equations. According to the deformation theory of thin plate, the deformation coordination control equation of the annular thin plate is derived [15, 16]:

$$\frac{\partial^4 w}{\partial r^4} + \frac{2}{r^2}\frac{\partial^4 w}{\partial r^2 \partial \theta^2} + \frac{1}{r^4}\frac{\partial^4 w}{\partial \theta^4} + \frac{2}{r}\frac{\partial^3 w}{\partial r^3} - \frac{2}{r^3}\frac{\partial^3 w}{\partial r \partial \theta^2} - \frac{1}{r^2}\frac{\partial^2 w}{\partial r^2} + \frac{4}{r^4}\frac{\partial^2 w}{\partial \theta^2} + \frac{1}{r^3}\frac{\partial w}{\partial r} = \frac{q(r,\theta,t)}{D}, \tag{1}$$

where w is the bending deflection, $q(r,\theta,t)$ is the uniform distribution force of a thin plate, and D is the bending stiffness given by

$$D = \frac{EH^3}{12(1-\nu^2)}, \tag{2}$$

in which H is the elastic thin plate thickness, E is Young's modulus, and ν is Poisson's ratio.

In dynamic analysis, the pressure distribution of the gas film is dependent on time, so it cannot be omitted. And in the low-speed state, negligible relative sliding speed, the general expression of gas lubrication control equation in polar coordinates is as follows:

$$\frac{1}{r}\frac{\partial}{\partial r}\left(h^3 r \frac{\partial p^2}{\partial r}\right) + \frac{1}{r^2}\frac{\partial}{\partial \theta}\left(h^3 \frac{\partial p^2}{\partial \theta}\right) = 12\mu \frac{\partial (ph)}{\partial t}, \tag{3}$$

where h is the gas film gap, p is the pressure distribution, μ is the dynamic viscosity, and t is the time.

When solving the gas lubrication control equation, the flow equilibrium condition should be satisfied:

$$Q_{\text{in}} = Q_{\text{out}}, \tag{4}$$

where

$$\begin{aligned}
Q_{\text{in}} &= AC_0\Psi \frac{p_s}{\sqrt{R_g T_0}}, \\
Q_{\text{out}} &= \frac{\gamma_a h^3}{12\mu}\int_0^{2\pi} \frac{\partial p}{\partial r} r\, d\theta, \\
\Psi &= \left\{2g\frac{k}{k-1}\left[\left(\frac{p_o}{p_s}\right)^{2/k} - \left(\frac{p_o}{p_s}\right)^{k-(1/k)}\right]\right\}^{1/2}, \quad \frac{p_o}{p_s} \geq \left(\frac{2}{k+1}\right)^{k/(k-1)}, \\
\Psi &= \left[2g\frac{k}{k-1}\left(\frac{2}{k+1}\right)^{2/(k-1)}\right]^{1/2}, \quad \frac{p_o}{p_s} < \left(\frac{2}{k+1}\right)^{k/(k-1)},
\end{aligned} \tag{5}$$

where Q_{in} is the mass flow in, Q_{out} is the mass flow out, g is the acceleration due to gravity, μ is the dynamic viscosity, p_o is the outlet pressure, p_s is the supply pressure, T_0 is the temperature, R_g is the gas constant, k is the adiabatic index, C_0 is the flow coefficient, d is the orifice diameter, and Ψ is the flow velocity coefficient.

Under the stable working condition, the gas film pressure of the bearing is equal to the load on the surface of the thin plate, so $q(r,\theta,t) = p$; then, (1), (3), and (4)

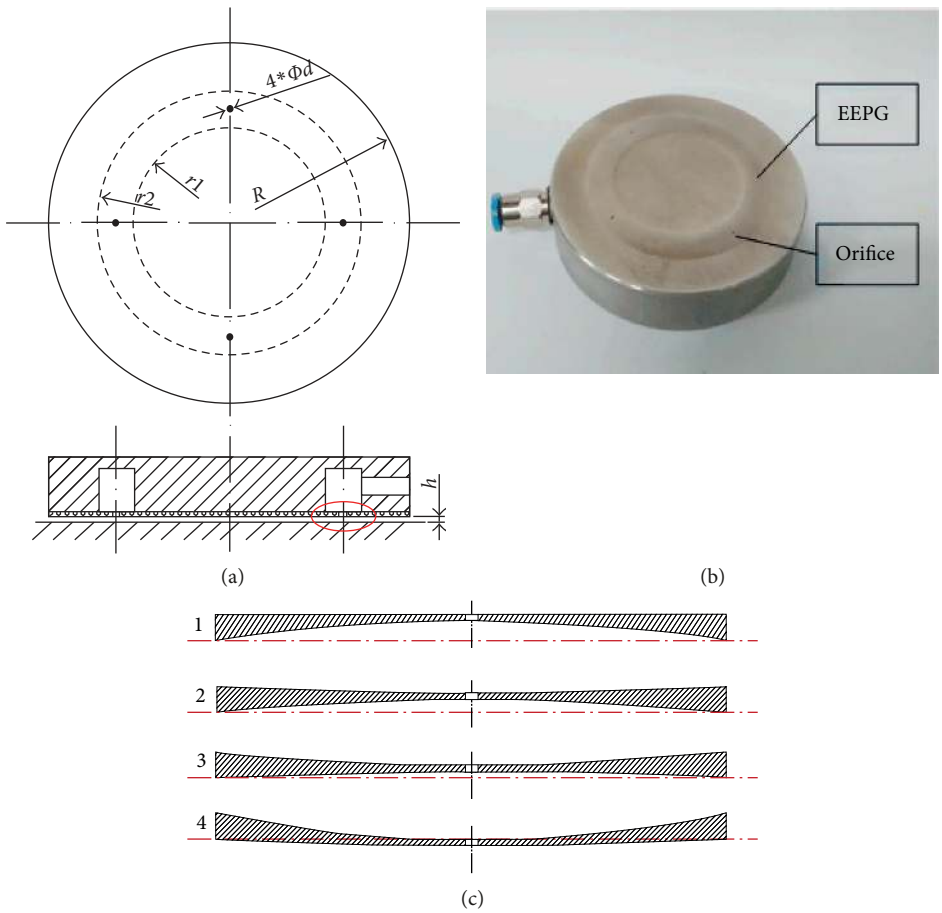

Figure 1: The new aerostatic bearing model with EEPG [15]. (a) Physical model. (b) Physical map. (c) Deformation of the EEPG.

constitute the dynamic gas-solid coupling control equation of the aerostatic bearing with the EEPG. Because the deformation of the EEPG is mainly affected by the pressure distribution of the gas film, the dynamic gas-solid coupling control equation is mainly for solving the gas lubrication control equation.

2.3. Perturbation Method for Solving the Control Equation of Gas Lubrication. Under the dynamic condition, the pressure distribution and the value of the gas film can be expressed by a steady value and a perturbation value:

$$\begin{aligned} p &= p_0 + \Delta p, \\ h &= h_0 + \Delta h, \end{aligned} \tag{6}$$

where p_0 is the pressure distribution at the steady state, h_0 is the gas film gap at the steady state, Δp is the perturbation value of pressure distribution, and Δh is the perturbation value of the gas film gap.

Formula (6) is introduced into (3), and the dynamic control equation of gas lubrication is obtained as follows:

$$\begin{aligned} &\frac{1}{r}\frac{\partial}{\partial r}\left(rh_0^3\frac{\partial p_0^2}{\partial r} + 2rh_0^3\frac{\partial p_0 \Delta p}{\partial r} + 3rh_0^2\Delta h\frac{\partial p_0^2}{\partial r}\right) \\ &\quad + \frac{1}{r^2}\frac{\partial}{\partial \theta}\left(h_0^3\frac{\partial p_0^2}{\partial \theta} + 2h_0^3\frac{\partial p_0 \Delta p}{\partial \theta} + 3h_0^2\Delta h\frac{\partial p_0^2}{\partial \theta}\right) \\ &\quad = 12\mu\frac{\partial}{\partial t}\left(p_0\Delta h + \Delta p h_0\right). \end{aligned} \tag{7}$$

On decomposing the steady term and the perturbation term in (7), they are as follows:

Steady term:

$$\frac{1}{r}\frac{\partial}{\partial r}\left(rh_0^3\frac{\partial p_0^2}{\partial r}\right) + \frac{1}{r^2}\frac{\partial}{\partial \theta}\left(h_0^3\frac{\partial p_0^2}{\partial \theta}\right) = 0. \tag{8}$$

Perturbation term:

$$\begin{aligned} &2\left(\frac{1}{r}\frac{\partial}{\partial r}\left(rh_0^3\frac{\partial p_0 \Delta p}{\partial r}\right) + \frac{1}{r^2}\frac{\partial}{\partial \theta}\left(h_0^3\frac{\partial p_0 \Delta p}{\partial \theta}\right)\right) \\ &\quad + 3\left(\frac{1}{r}\frac{\partial}{\partial r}\left(rh_0^2\Delta h\frac{\partial p_0^2}{\partial r}\right) + \frac{1}{r^2}\frac{\partial}{\partial \theta}\left(h_0^2\Delta h\frac{\partial p_0^2}{\partial \theta}\right)\right) \\ &\quad = 12\mu\frac{\partial}{\partial t}\left(p_0\Delta h + \Delta p h_0\right). \end{aligned} \tag{9}$$

The complex number expression form of Δp and Δh is

$$\Delta h = \varepsilon h_0 e^{j\omega t}, \quad \Delta p = \varepsilon p_\delta e^{j\omega t}, \tag{10}$$

where ε is a perturbation, p_δ is the dynamic variation of pressure distribution, h_0 is the gas film gap at the steady state, ω is the perturbed frequency, and $j = \sqrt{-1}$.

Formula (10) is introduced into (9) to obtain the following equation:

$$\frac{h_0^2}{r}\frac{\partial p_0 p_\delta}{\partial r} + h_0^2\frac{\partial^2 p_0 p_\delta}{\partial r^2} + \frac{h_0^2}{r^2}\frac{\partial^2 p_0 p_\delta}{\partial \theta^2} = j\frac{6\mu\omega\left(p_0^2 + p_0 p_\delta\right)}{p_0}. \tag{11}$$

Then, (11) is the complex number expression form of the perturbation Reynolds equation.

For the convenience of calculation, suppose

$$p_0 p_\delta = p_A + j p_B, \tag{12}$$

where p_A is the real part, p_B is the imaginary part, and $j = \sqrt{-1}$.

Formula (12) is introduced into (11), and the real part and the imaginary part are arranged, respectively, to obtain the following equation:

$$\begin{aligned} &\frac{1}{r}\frac{\partial p_A}{\partial r} + \frac{\partial^2 p_A}{\partial r^2} + \frac{1}{r^2}\frac{\partial^2 p_A}{\partial \theta^2} = -\frac{6\mu p_B \omega}{p_0 h_0^2}, \\ &\frac{1}{r}\frac{\partial p_B}{\partial r} + \frac{\partial^2 p_B}{\partial r^2} + \frac{1}{r^2}\frac{\partial^2 p_B}{\partial \theta^2} = \frac{6\mu\left(p_A + p_0^2\right)\omega}{p_0 h_0^2}. \end{aligned} \tag{13}$$

In summary, the dynamic gas lubrication control equation can be decomposed into a steady term (8) and a perturbation term (13).

2.4. Calculation Method of the Perturbation Equation. The finite difference method is used to discretize (13). The difference scheme is as follows:

$$\begin{aligned} &\frac{\partial p_0}{\partial r} = \frac{p_0(i+1,j) - p_0(i-1,j)}{2\Delta r}, \\ &\frac{\partial p_0}{\partial \theta} = \frac{p_0(i,j+1) - p_0(i,j-1)}{2\Delta \theta}, \\ &\frac{\partial p_A}{\partial r} = \frac{p_A(i+1,j) - p_A(i-1,j)}{2\Delta r}, \\ &\frac{\partial p_A}{\partial \theta} = \frac{p_A(i,j+1) - p_A(i,j-1)}{2\Delta \theta}, \\ &\frac{\partial p_B}{\partial r} = \frac{p_B(i+1,j) - p_B(i-1,j)}{2\Delta r}, \\ &\frac{\partial p_B}{\partial \theta} = \frac{p_B(i,j+1) - p_B(i,j-1)}{2\Delta \theta}, \\ &\frac{\partial^2 p_A}{\partial r^2} = \frac{p_A(i+1,j) - 2p_A(i,j) + p_A(i-1,j)}{\Delta r^2}, \\ &\frac{\partial^2 p_A}{\partial \theta^2} = \frac{p_A(i,j+1) - 2p_A(i,j) + p_A(i,j-1)}{\Delta \theta^2}, \\ &\frac{\partial^2 p_B}{\partial r^2} = \frac{p_B(i+1,j) - 2p_B(i,j) + p_B(i-1,j)}{\Delta r^2}, \\ &\frac{\partial^2 p_B}{\partial \theta^2} = \frac{p_B(i,j+1) - 2p_B(i,j) + p_B(i,j-1)}{\Delta \theta^2}, \\ &\frac{\partial^2 p_0}{\partial r^2} = \frac{p_0(i+1,j) - 2p_0(i,j) + p_0(i-1,j)}{\Delta r^2}, \\ &\frac{\partial^2 p_0}{\partial \theta^2} = \frac{p_0(i,j+1) - 2p_0(i,j) + p_0(i,j-1)}{\Delta \theta^2}. \end{aligned} \tag{14}$$

Formula (14) is introduced into (13), and a formula of super relaxation for iterative calculation is obtained:

$$\begin{aligned} p_A^{k+1}(i,j) &= p_A^k(i,j) + \alpha\left[A(i,j) - p_A^k(i,j)\right], \\ p_B^{k+1}(i,j) &= p_B^k(i,j) + \alpha\left[B(i,j) - p_B^k(i,j)\right], \end{aligned} \tag{15}$$

where

$$\begin{aligned} p_A(i,j) &= \frac{(1/r)\left(\left(p_A(i+1,j) - p_A(i-1,j)\right)/(2\Delta r)\right) + \left(p_A(i+1,j) + p_A(i-1,j)\right)/(\Delta r^2) + (1/r^2)\left(\left(p_A(i,j+1) + p_A(i,j-1)\right)/\left(\Delta\theta^2\right)\right) + \left(6\mu p_B\omega\right)/\left(p_0 h_0^2\right)}{\left((2/\Delta r^2) + \left(2/r^2\Delta\theta^2\right)\right)}, \\ p_B(i,j) &= \frac{(1/r)\left(\left(p_B(i+1,j) - p_B(i-1,j)\right)/(2\Delta r)\right) + \left(p_B(i+1,j) + p_B(i-1,j)\right)/(\Delta r^2) + (1/r^2)\left(\left(p_B(i,j+1) + p_B(i,j-1)\right)/\left(\Delta\theta^2\right)\right) - \left(6\mu\left(p_A + p_0^2\right)\omega\right)/\left(p_0 h_0^2\right)}{\left((2/\Delta r^2) + \left(2/r^2\Delta\theta^2\right)\right)}, \end{aligned} \tag{16}$$

and α is the convergence coefficient, which is generally in the range $0 < \alpha < 1$.

2.5. Dynamic Characteristic Analysis. The dynamic characteristics of the aerostatic bearing include dynamic stiffness and equivalent damping coefficient. In order to calculate the dynamic characteristics of the aerostatic bearing, the static pressure distribution p_0 at the working point is calculated according to (1) and the steady term of (4) and (8). Secondly, the calculated p_0 as a known parameter is introduced into (13), and p_A and p_B in the coupled partial differential

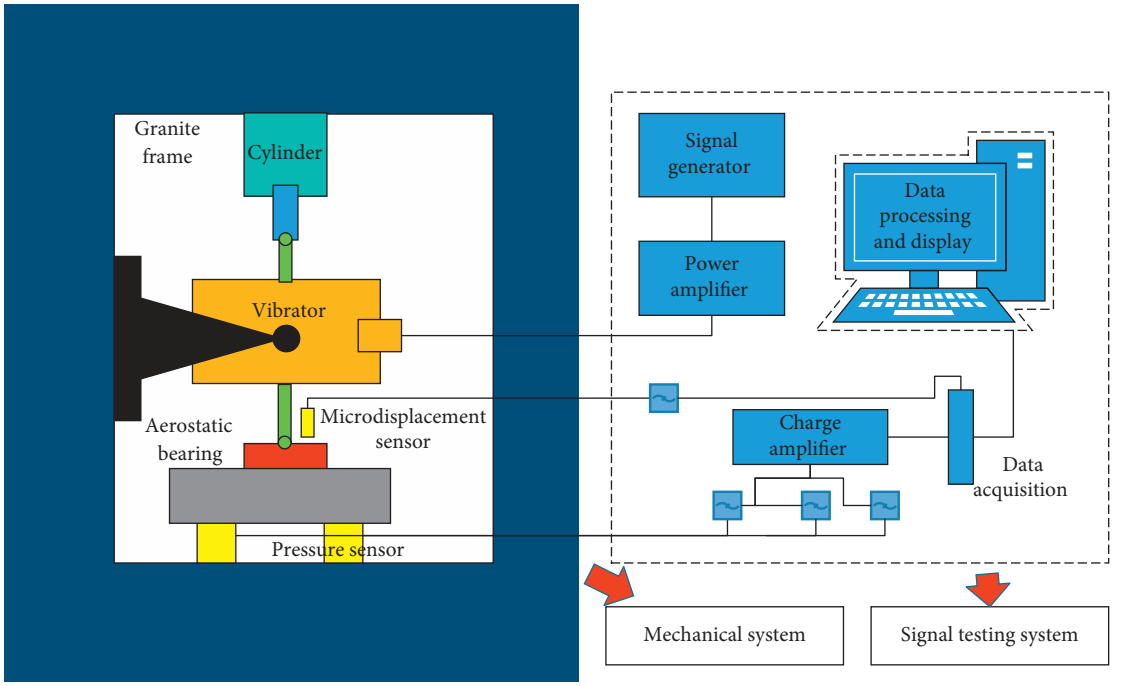

(a)

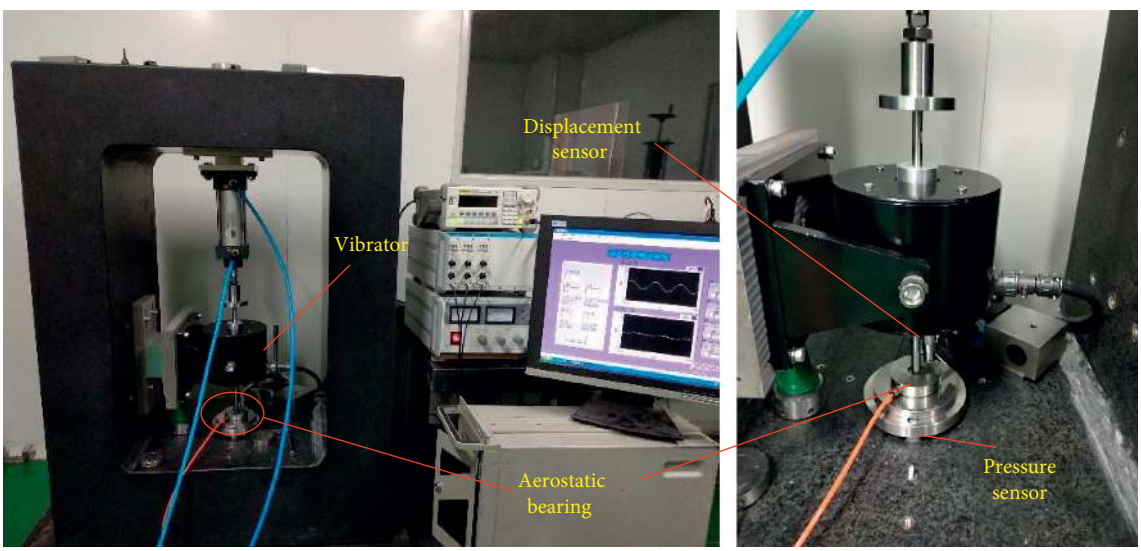

(b)

Figure 2: (a) Principle diagram of the dynamic test rig. (b) Physical map of the dynamic test rig.

equations are calculated; thus, the dynamic pressure distribution p_δ of the gas film at the working point can be obtained. Through (10), the dynamic pressure Δp is introduced into (1) and the deformation of the thin plate under the micro-perturbation is calculated; p_0 of the static pressure distribution is corrected, and the perturbation (13) is calculated again. If the difference between the values calculated by p_A and p_B two times is less than 1×10^{-6}, the coupling ends. Finally, the pressure distribution of the gas film is integrated, and the bearing capacity of the gas film can be obtained:

$$W = W_0 + \varepsilon W_1 e^{j\omega t}, \tag{17}$$

where

$$W_1 = \iint p_\delta r \, dr \, d\theta, \tag{18}$$

and W_0 is the bearing capacity of the gas film in the steady state.

Ignoring the higher-order infinitesimal, the Taylor expansion of bearing capacity of the gas film at equilibrium position can be expressed as follows:

$$W = W_0 + \frac{\partial W_0}{\partial h} \Delta h + \frac{\partial W_0}{\partial \dot{h}} \Delta \dot{h}, \tag{19}$$

Table 1: Numerical calculation parameters.

Parameters	H (mm)	R (mm)	$r1$ (mm)	$r2$ (mm)	d (mm)	E (GPa)	ε	P_a (MPa)	C_0
Value	0.3	30	15	25	0.3	1.12	0.1	0.1	$C_0 = 0.85 \times (1 - e^{-8.2}(w + h))$ [3]
Parameters	g	ν	R_g	μ (Pa·s)	T_0 (K)	k	P_s (MPa)	γ_a (kg/m^3)	α
Value	9.8	0.3	29.27	1.883×10^{-5}	300	1.4	0.5	1.226	0.25

where Δh and $\Delta \dot{h}$ are the displacement perturbation and velocity perturbation of the gas film direction, respectively.

Combining (17) and (19), the following equation can be obtained:

$$\varepsilon W_1 e^{j\omega t} = K\Delta h + C\Delta \dot{h}. \tag{20}$$

Formula (10) is introduced into (20), and the real part and the imaginary part of (20) are separated. The dynamic stiffness K and the equivalent damping coefficient C of the aerostatic bearing with the EEPG are obtained:

$$K = -\frac{\mathrm{Re}(W_1)}{h_0}, \qquad C = -\frac{\mathrm{Im}(W_1)}{\omega h_0}. \tag{21}$$

3. Experimental Verification

3.1. Experimental Rig Construction. The test rig for the bearing dynamic performance test is shown in Figure 2. The experimental rig is composed of two parts: the mechanical system and the signal test system. The mechanical system is made up of the granite frame, cylinder, vibration exciter, microdisplacement sensor, measured aerostatic bearing, and dynamic pressure sensor. The signal test system is composed of the signal generator, power amplifier, charge amplifier, data acquisition device, and data processing and display device.

In order to avoid the test error caused by the stiffness of the test rig and ensure the accuracy of the dynamic test of the aerostatic bearing, we chose the complete granite as the experimental framework. The bearing preload force is provided by the cylinder, and the continuous preload is the output provided by changing the cylinder pressure. The maximum output preload is 2000 N.

The vibrator (JZK-10) uses a two-way joint to connect the cylinder and the bearing so that the bearing can get a dynamic exciting force at a certain frequency. The maximum output force is 100 N, and the maximum excitation frequency is 1000 Hz.

The dynamic force sensor (CL-YD-312), which is uniformly distributed by 3 parts, is used to output the change of the gas film pressure. And the minimum resolution is 0.1 N. The noncontact capacitive displacement sensor (DWS) is used to test the change of the gas film gap. The accuracy of the test is 0.01 μm, which ensures the accuracy of the test.

In dynamic testing, first, the signal generator produces a certain frequency sinusoidal excitation, through the power amplifier (YE5782A) to the vibrator, so that the vibrator produces a certain frequency exciting force. Then, the exciting force passes through the guide rod to the measured aerostatic bearing, and the gas film is subjected to periodic extrusion. The dynamic change signals of the gas film displacement and gas film force are measured by the microdisplacement sensor and the dynamic pressure sensor, respectively. Finally, the data obtained from the test are processed and displayed by the LabVIEW multisignal.

3.2. Experimental Data Processing Method. The time signal of exciting force and displacement is obtained through acquisition and test. By means of signal processing, a series of data of the bearing gas film force variation, relative displacement, and relative velocity of the bearing are obtained. Finally, the dynamic stiffness and the equivalent damping coefficient of the bearing are obtained by the least squares method [5]. Under the microperturbation, the variation of the theoretical gas film force $\Delta \widetilde{W}_1$ of the bearing can be expressed as a function of the displacement Δh and velocity $\Delta \dot{h}$ of the aerostatic bearing deviating from the steady working point, which is expressed as follows:

$$\Delta \widetilde{W}_1 = K\Delta h + C\Delta \dot{h}. \tag{22}$$

The actual measured dynamic gas film force of the bearing can be expressed as ΔW_{test}.

The n group data of dynamic displacement and gas film force of the aerostatic bearing are tested under a certain excitation frequency. According to the least squares principle, there is a minimum sum of squares between the variation of the theoretical gas film force and the actual measured value:

$$\min \xi^2 = \sum_{i=1}^{n} \left(\Delta \widetilde{W}_{1i} - \Delta W_{i\text{test}}\right)^2. \tag{23}$$

According to the multivariate function extreme value theory,

$$\frac{\partial \xi^2}{\partial K} = 0, \qquad \frac{\partial \xi^2}{\partial C} = 0. \tag{24}$$

Formula (23) is introduced into (24), to obtain the following equation:

$$\begin{bmatrix} \sum_{i=1}^{n} \Delta h_i^2 & \sum_{i=1}^{n} \Delta h_i \Delta \dot{h}_i \\ \sum_{i=1}^{n} \Delta h_i \Delta \dot{h}_i & \sum_{i=1}^{n} \Delta \dot{h}_i^2 \end{bmatrix} \begin{bmatrix} K \\ C \end{bmatrix} = \begin{bmatrix} \sum_{i=1}^{n} \Delta h_i \Delta W_{1i} \\ \sum_{i=1}^{n} \Delta \dot{h}_i \Delta W_{1i} \end{bmatrix}. \tag{25}$$

Finally, the dynamic stiffness and the equivalent damping coefficient of the aerostatic bearing are obtained through processing the test signals.

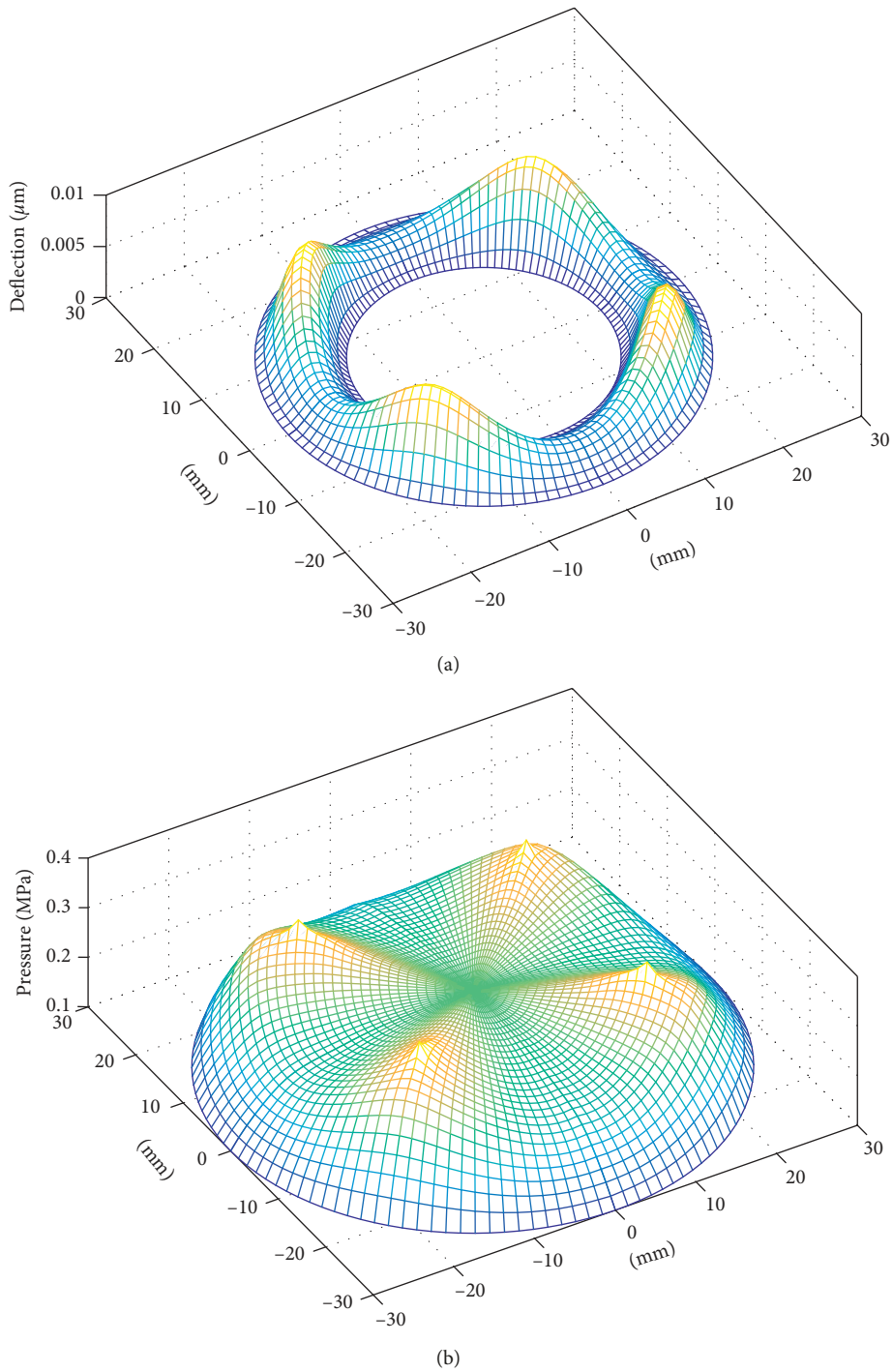

Figure 3: Static characteristics of the aerostatic bearing with EEPG ($h = 8$ m). (a) Deformation diagram of EEPG. (b) Gas film pressure distribution diagram.

4. Results and Discussion

4.1. Numerical Calculation Results. The mathematical model established in this paper is numerically solved, and the calculated parameters are shown in Table 1.

First, the static pressure distribution p_0 of the aerostatic bearing with EEPG is calculated. Figure 3 shows the static characteristic of the aerostatic bearing with EEPG when the gas film gap h is equal to 8 μm. Figure 3(a) shows the deformation diagram of EEPG, and Figure 3(b) shows the gas film pressure distribution diagram. The static calculation of pressure distribution p_0 is used as the initial condition to solve the perturbation equation of the gas lubrication control equation. The dynamic stiffness and equivalent damping coefficient of the bearing with EEPG are obtained. The calculation results are shown in Figures 4 and 5.

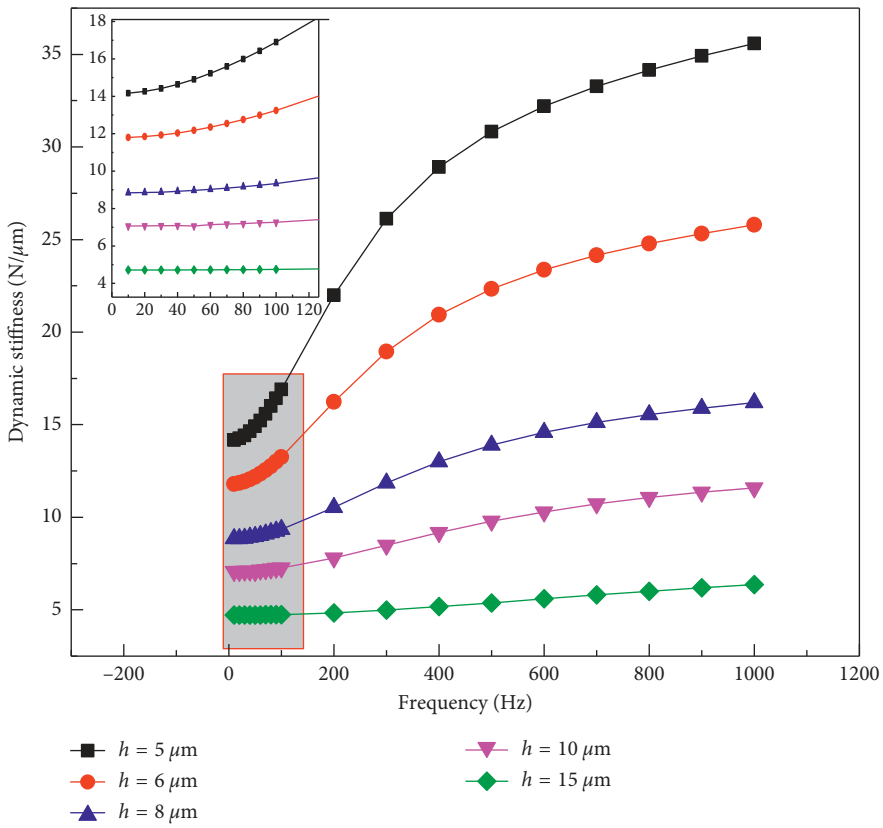

(a)

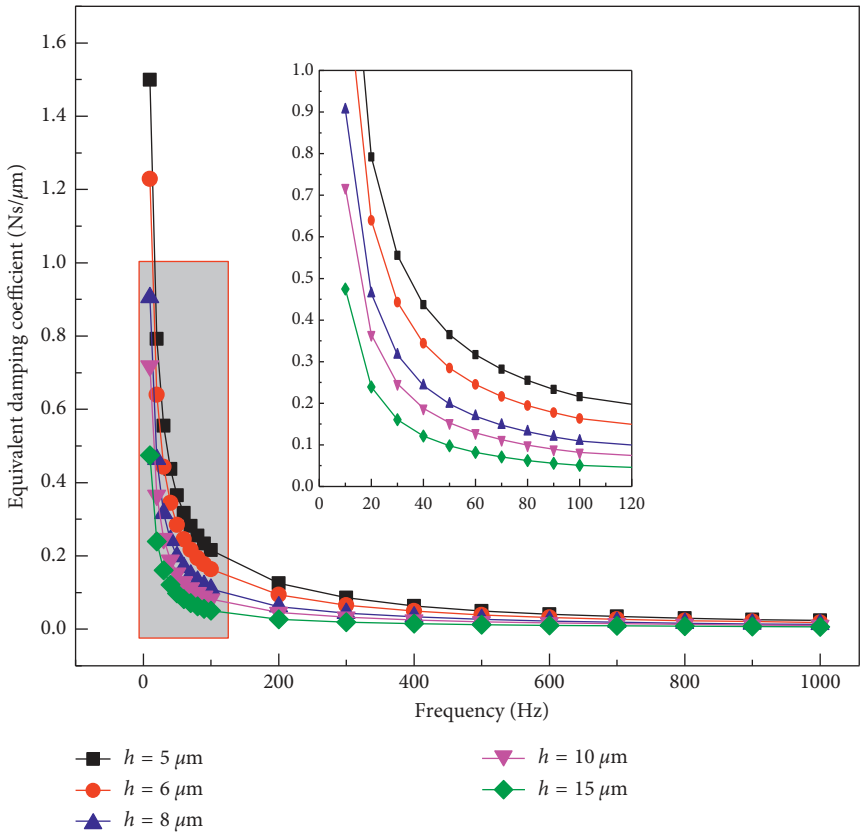

(b)

Figure 4: Influence of the perturbation frequency on dynamic characteristics of aerostatic bearings with EEPG. (a) Influence of the disturbance frequency on the dynamic stiffness. (b) Influence of the disturbance frequency on the equivalent damping coefficient.

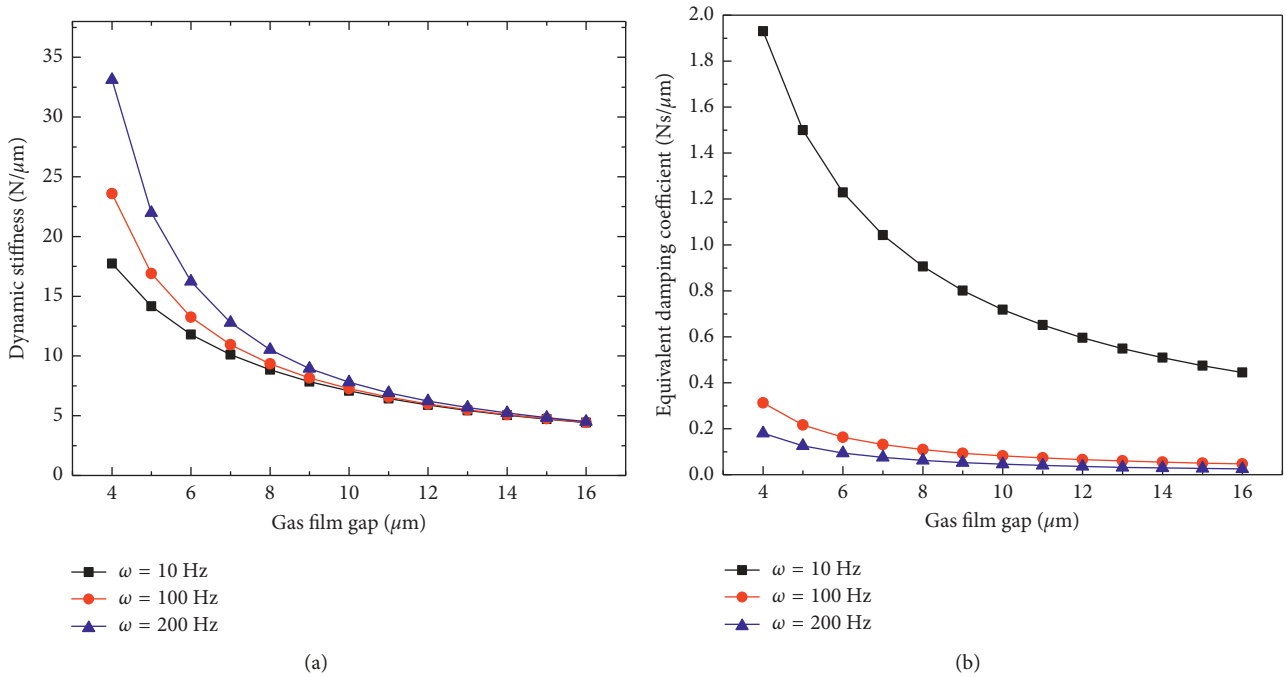

Figure 5: Influence of the gas film gap on dynamic characteristics of aerostatic bearings with EEPG. (a) Influence of the gas film gap on dynamic stiffness. (b) Influence of the gas film gap on the equivalent damping coefficient.

Figure 4 shows the influence of the perturbation frequency on dynamic characteristics of aerostatic bearings with EEPG. As shown in Figure 4(a), at the same gas film gap h, the dynamic stiffness K of the aerostatic bearing increases with the increase of the perturbation frequency ω. For example, the gas film gap h is equal to 8 μm: when the perturbation frequency ω is equal to 200 Hz, the dynamic stiffness of the bearing is equal to 11 N/μm. When the perturbation frequency ω is increased to 1000 Hz, the dynamic stiffness K of the bearing is equal to 16 N/m. Under the same perturbation frequency ω, the smaller the h of the gas film gap is, the greater the dynamic stiffness K of the bearing is. For example, the perturbation frequency ω is equal to 400 Hz: when the gas film gap h is equal to 5 μm, the dynamic stiffness K of the bearing is equal to 27 N/μm; when [[parms resize(1),pos(50,50),size(200,200),bgcol(156)]]e gas film gap h. When the perturbation frequency $\omega < 200$ Hz, the equivalent damping coefficient C decreases most obviously; when the perturbation frequency $\omega > 200$ Hz, the equivalent damping coefficient C decreases more slowly, until it approaches 0. For example, the gas film gap h is equal to 8 μm: when the perturbation frequency ω is equal to 200 Hz, the equivalent damping coefficient C of the bearing is equal to 0.0618 Ns/μm; when the perturbation frequency ω increases to 1000 Hz, the equivalent damping coefficient C is equal to 0.0129 Ns/μm. Under the same perturbation frequency ω, the smaller the gas film gap h is, the greater the equivalent damping coefficient C is. For example, the perturbation frequency ω is equal to 300 Hz: when the gas film gap h is equal to 5 μm, the equivalent damping coefficient C of the bearing is equal to 0.0857 Ns/μm; when the gas film gap h is equal to 10 μm, the equivalent damping coefficient of the bearing is equal to 0.0323 Ns/μm; when the gas film gap h is equal to 15 μm, the equivalent damping number of the bearing is equal to 0.0189 Ns/μm.

Figure 5 shows the influence of the gas film gap on dynamic characteristics of aerostatic bearings with EEPG. It can be seen from Figure 5(a) that, at the same perturbation frequency ω, the dynamic stiffness K of the aerostatic bearing decreases with the increase of the gas film gap h. For example, the perturbation frequency ω is equal to 10 Hz: when the gas film gap h is equal to 4 μm, the dynamic stiffness K of the bearing is equal to 33 N/μm; when the gas film gap h increases to 16 μm, the dynamic stiffness K of the bearing is equal to 4.9 N/μm. Moreover, when the film gap $h < 10$ μm, the dynamic stiffness of bearings decreases faster. When the gas film gap $h > 10$ μm, the dynamic stiffness of bearings decreases more slowly. At the same gas film gap, the greater the perturbation frequency ω, the greater the dynamic stiffness K of the bearing. But with the increase of the gas film gap h, the influence of the disturbance frequency ω on the dynamic stiffness K is weakened until there is no effect. For example, the gas film gap h is equal to 4 μm: when the perturbation frequency ω is equal to 200 Hz, the dynamic stiffness K of the bearing is equal to 33 N/μm; when the perturbation frequency ω is equal to 100 Hz, the dynamic stiffness K of the bearing is equal to 24 N/μm. When the gas film gap h is equal to 16 μm, the dynamic stiffness K of the bearing is equal to 4.9 N/μm, no matter how the perturbation frequency K is. From Figure 5(b), we can see that, at the same perturbation frequency ω, the equivalent damping C of the aerostatic bearing decreases with the increase of the gas film gap h. For example, the perturbation frequency ω is equal to 10 Hz: when the gas film gap h is equal to 4 μm, the equivalent damping coefficient C of the bearing is equal to 1.93 Ns/μm; when the gas film gap h is equal to 16 μm, the

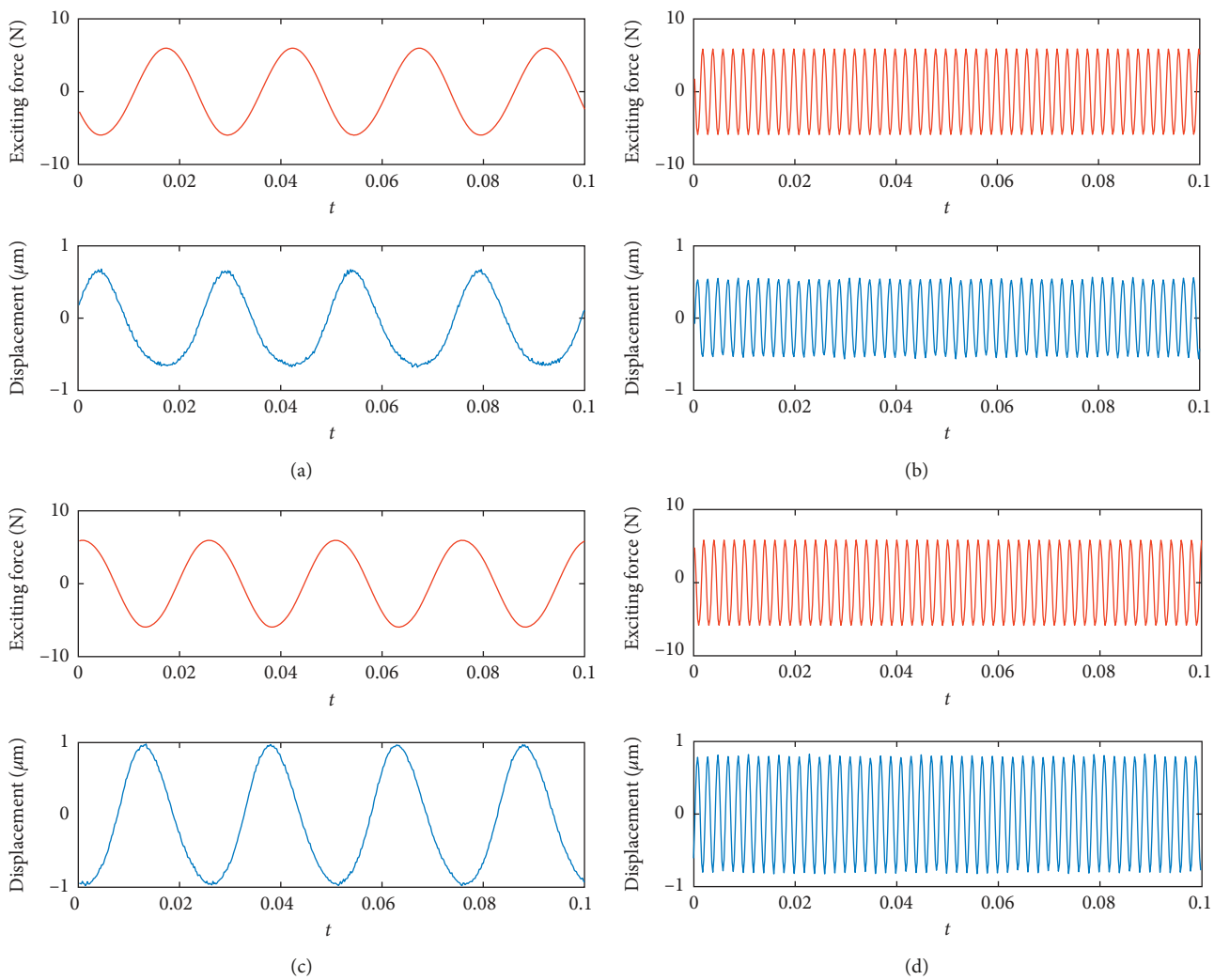

Figure 6: Dynamic gas film force and dynamic displacement under different perturbation frequencies: (a) $\omega = 40$ Hz; (b) $\omega = 500$ Hz; (c) $\omega = 40$ Hz; (d) $\omega = 500$ Hz.

equivalent damping coefficient C of the bearing is equal to 0.5 Ns/μm. At the same gas film gap h, the larger the perturbation frequency ω is, the smaller the equivalent damping coefficient C of the bearing is, and it can be seen that the perturbation frequency ω has obvious influence on the equivalent damping coefficient C in the interval of 10~100 Hz. For example, the gas film gap h is equal to 4 μm: when the perturbation frequency ω is equal to 100 Hz, the equivalent damping coefficient C of the bearing is equal to 0.3 Ns/μm; when the perturbation frequency ω is equal to 200 Hz, the equivalent damping coefficient C of the bearing is equal to 0.2 Ns/μm. When the perturbation frequency ω is in the range of 10~100 Hz, the variation of the equivalent damping coefficient C is equal to 1.63 Ns/μm. And when the perturbation frequency ω is in the range of 100~200 Hz, the change of the equivalent damping coefficient C of the bearing is only 0.1 Ns/μm.

4.2. Experimental Test Results. In the experimental test, the amplitude of the output force of the exciting force is 6 N, the excitation frequency is 40~500 Hz, and the sampling frequency is 10000 Hz. Figure 6 shows the dynamic load and dynamic displacement of aerostatic bearings in 0.1 s at different excitation frequencies when the steady gas film gap h is equal to 10 μm and 15 μm.

Figure 7 shows the experimental test data. Figures 7(a) and 7(b) show numerical calculations and experimental comparison diagrams for the dynamic performance of bearings when the steady gas film gap is equal to 10 μm. Figures 7(c) and 7(d) show comparison diagrams for the steady gas film gap equal to 15 μm. From Figure 7, it can be seen that the experimental test and the numerical calculation are consistent. The dynamic stiffness increases with the increase of frequency, and the equivalent damping coefficient decreases with the increase of frequency. The dynamic stiffness of the test is slightly larger than that of the numerical calculation. The equivalent damping coefficient of the experimental test is basically the same as that of the theoretical calculation.

The main error in the experiment is the bearing accuracy, the measurement equipment error, and resonance. In the

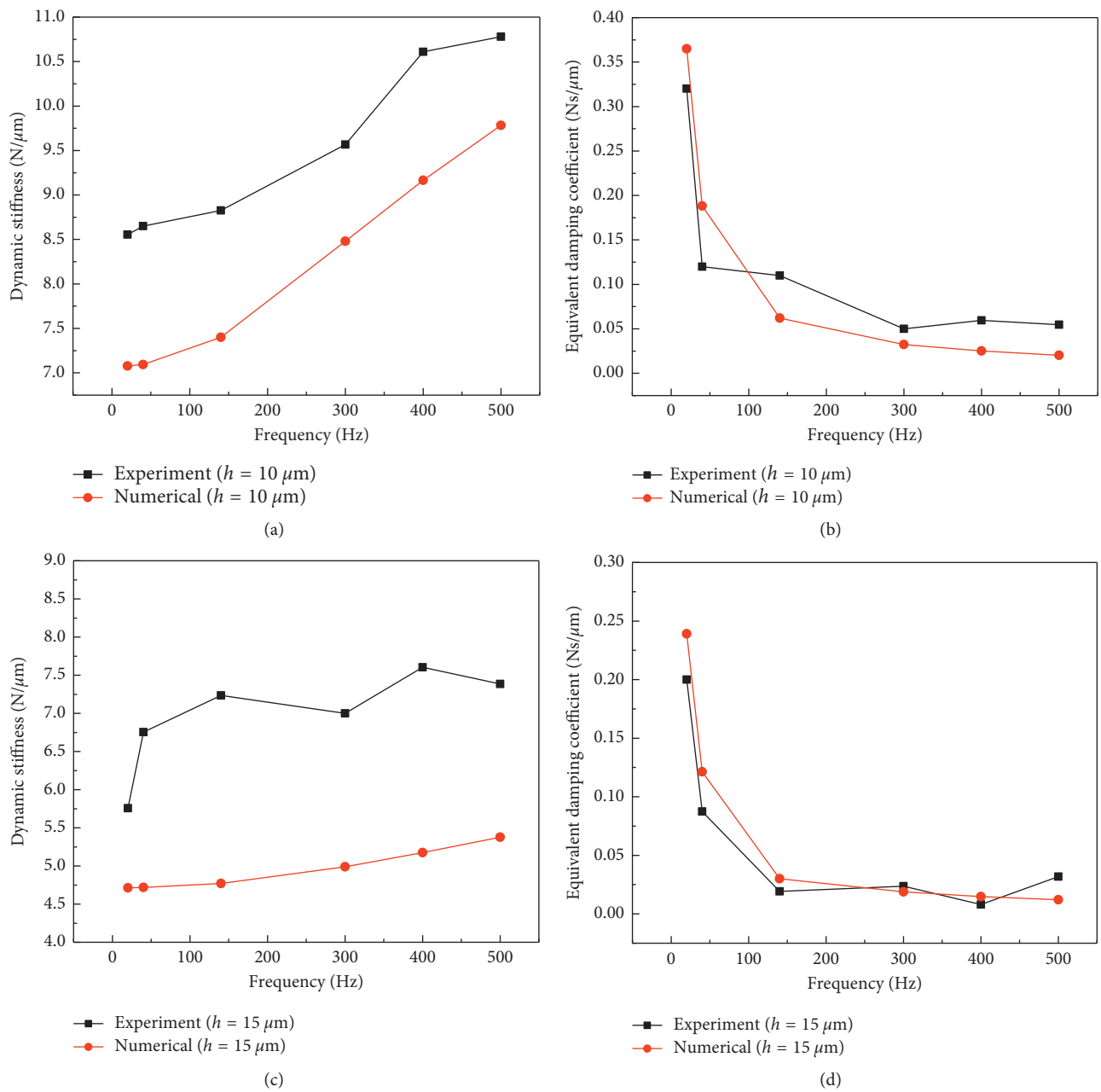

Figure 7: Experimental test data: (a) dynamic stiffness at $h = 10\,\mu$m; (b) equivalent damping coefficient at $h = 10\,\mu$m; (c) dynamic stiffness at $h = 15\,\mu$m; (d) equivalent damping coefficient at $h = 15\,\mu$m.

experiment, we should try to improve the geometric machining error of the aerostatic bearing, adopt the high-accuracy test equipment, and avoid the resonance interval of the dynamic test rig. Through a large number of experimental tests, the test data are analyzed, eliminated, and compensated to improve the reliability of dynamic testing.

5. Conclusion

In this paper, the dynamic characteristics of the aerostatic bearing with EEPG are studied by numerical calculation and experimental method. The following conclusions are obtained:

(1) At the same gas film gap (or the same load), the perturbation frequency has an important influence on the dynamic performance of the aerostatic bearing with EEPG. With the increase of perturbation frequency, the dynamic stiffness of the bearing increases and the equivalent damping coefficient of the bearing decreases. The smaller the gas film gap, the greater the dynamic stiffness of the bearing and the greater the equivalent damping coefficient.

(2) At the same perturbation frequency, the dynamic stiffness of the aerostatic bearing decreases with the increase of the gas gap and the equivalent damping

coefficient decreases. The larger the perturbation frequency is, the smaller the dynamic stiffness and the equivalent damping coefficient of the bearing are.

(3) In application, to get better dynamic performance, high-frequency vibration should be avoided. The optimization of the dynamic characteristics of the new aerostatic bearing will be studied in the future.

Data Availability

The data used to support the findings of this study are available from the corresponding author upon request.

Conflicts of Interest

The authors declare that they have no conflicts of interest.

Acknowledgments

The authors would like to acknowledge that the project was supported by the National Natural Science Foundation of China (51705390), Xi'an Weiyang Science and Technology Project (201838), Xi'an Science and Technology Planning Project 2017075CG/RC038(XAGY008), and Xi'an Technological University Gas Lubrication Research and Innovation Team Construction Project.

References

[1] W. Ma and D. Li, "CFD investigation of an aerostatic thrust bearing flow field with new type of throttling structure," *Journal of Convergence Information Technology*, vol. 7, no. 18, pp. 540–548, 2012.

[2] D. Ghodsiyeh, F. Colombo, T. Raparelli, A. Trivella, and V. Viktorov, "Diaphragm valve-controlled air thrust bearing," *Tribology International*, vol. 109, pp. 328–335, 2017.

[3] G. Belforte, T. Raparelli, V. Viktorov, and A. Trivella, "Discharge coefficients of orifice-type restrictor for aerostatic bearings," *Tribology International*, vol. 40, no. 3, pp. 512–521, 2007.

[4] H. Dong, X.-L. Zhao, and J.-A. Zhang, "Static characteristic analysis and experimental research of aerostatic thrust bearing with annular elastic uniform pressure plate," *Advances in Mechanical Engineering*, vol. 7, no. 3, pp. 1–13, 2015.

[5] H. Zhou, S. Zhao, H. Xu, and J. Zhu, "An experimental study on oil-film dynamic coefficients," *Tribology International*, vol. 37, no. 3, pp. 245–253, 2004.

[6] U. Nishio, K. Somaya, and S. Yoshimoto, "Numerical calculation and experimental verification of static and dynamic characteristics of aerostatic thrust bearings with small feedholes," *Tribology International*, vol. 44, no. 12, pp. 1790–1795, 2011.

[7] S. K. Yadav, A. K. Rajput, N. Ram, and S. C. Sharma, "A novel technique to compute static and dynamic performance characteristics of aerostatic thrust bearing," *Industrial Lubrication and Tribology*, vol. 70, no. 1, pp. 84–96, 2018.

[8] H. Cui, X. Yue, L. Zhang et al., "Static and dynamic characteristics of aerostatic bearing based on numerical simulation," *Journal of Mechanical Engineering*, vol. 52, no. 9, p. 116, 2016.

[9] L. Guo, "Finite element analysis the dynamic characteristics of static-pressure spherical gas bearings with inherent compensation," *China Mechanical Engineering*, vol. 15, no. 23, pp. 2069–2073, 2004.

[10] X. D. Chen, J. C. Zhu, and H. Chen, "Dynamic characteristics of ultra-precision aerostatic bearings," *Advances in Manufacturing*, vol. 1, no. 1, pp. 82–86, 2013.

[11] P. Yu, X. Chen, X. Wang, and W. Jiang, "Frequency-dependent nonlinear dynamic stiffness of aerostatic bearings subjected to external perturbations," *International Journal of Precision Engineering and Manufacturing*, vol. 16, no. 8, pp. 1771–1777, 2015.

[12] S. J. Zhang, S. To, C. F. Cheung, and H. T. Wang, "Dynamic characteristics of an aerostatic bearing spindle and its influence on surface topography in ultra-precision diamond turning," *International Journal of Machine Tools and Manufacture*, vol. 62, no. 1, pp. 1–12, 2012.

[13] L. U. Zhi-Wei, M. A. Fang-Jie, L. Bo et al., "Research on dynamic characteristics of aerostatic thrust bearings based on perturbation method," *Acta Armamentarii*, 2016.

[14] W. Ma, J. Cui, Y. Liu, and J. Tan, "Improving the pneumatic hammer stability of aerostatic thrust bearing with recess using damping orifices," *Tribology International*, vol. 103, pp. 281–288, 2016.

[15] Z. Xiao-long, Z. Jun-an, D. Hao, F. Zhou, and L. Jun-ning, "Numerical simulation and experimental study on the gas-solid coupling of the aerostatic thrust bearing with elastic equalizing pressure groove," *Shock and Vibration*, vol. 2017, Article ID 5091452, 11 pages, 2017.

[16] H. W. Liu, *Theory of Plate and Shells*, Zhejiang University Press, Zhejiang, China, 1987.

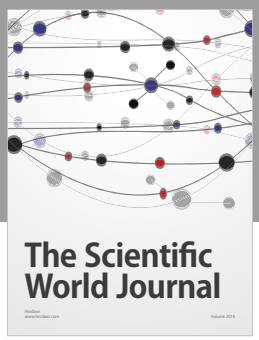

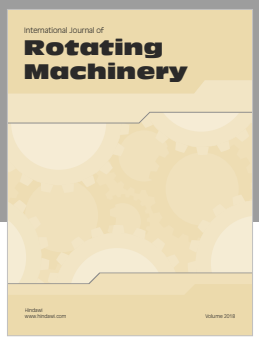

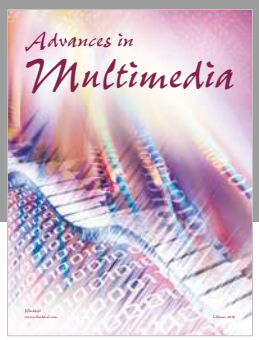

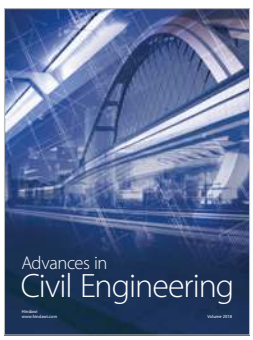

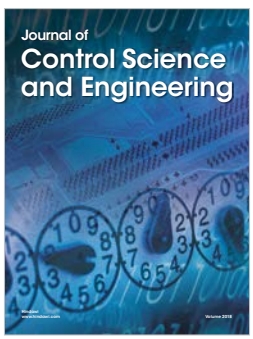

Hindawi
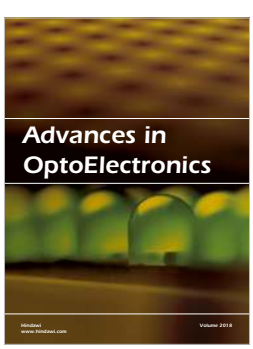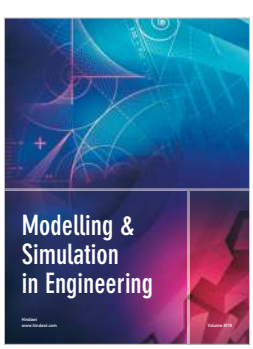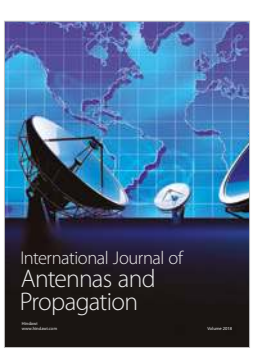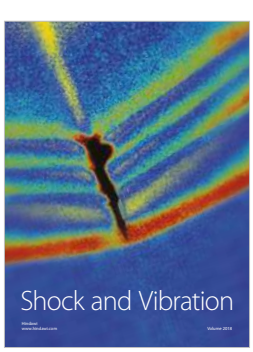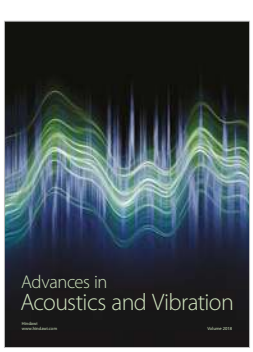
Submit your manuscripts at
www.hindawi.com